JOURNAL OF APPLIED CRYSTALLOGRAPHY
ISSN 1600-5767

Texture measurements on quartz single crystals to validate coordinate systems for neutron time-of-flight texture analysis

Matthew M. Schmitt,[a,b] Daniel J. Savage,[b] John D. Yeager,[b] Hans-Rudolf Wenk,[c] Luca Lutterotti[d] and Sven C. Vogel[b]*

[a]New Mexico Institute of Mining and Technology, Socorro, NM 87801, USA, [b]Los Alamos National Laboratory, Los Alamos, NM 87545, USA, [c]Department of Earth and Planetary Science, University of California, Berkeley, Berkeley, CA 94720, USA, and [d]Department of Industrial Engineering, University of Trento, Trento 38123, Italy. *Correspondence e-mail: sven@lanl.gov

Received 8 March 2023
Accepted 22 October 2023

Edited by J. Keckes, Montanuniversität Leoben, Austria

Dedicated to the memory of Professor Siegfried Matthies, a pioneer in texture analysis, who passed away on 24 February 2023.

Keywords: texture; neutron diffraction; coordinate systems.

Supporting information: this article has supporting information at journals.iucr.org/j

In crystallographic texture analysis, ensuring that sample directions are preserved from experiment to the resulting orientation distribution is crucial to obtain physical meaning from diffraction data. This work details a procedure to ensure instrument and sample coordinates are consistent when analyzing diffraction data with a Rietveld refinement using the texture analysis software *MAUD*. A quartz crystal is measured on the HIPPO diffractometer at Los Alamos National Laboratory for this purpose. The methods described here can be applied to any diffraction instrument measuring orientation distributions in polycrystalline materials.

1. Introduction

Polycrystalline materials are agglomerates of grains with different crystallographic orientations (Gilmore *et al.*, 2019). Texture measurements aim to determine the orientation distribution of grains in a bulk material (Kocks *et al.*, 1998; Wenk & Van Houtte, 2004). Time-of-flight (TOF) neutron diffraction has been applied for texture analysis by several facilities including HIPPO (High Pressure – Preferred Orientation) at Los Alamos National Laboratory, NM, USA (Wenk *et al.*, 2003; Vogel *et al.*, 2004); SKAT at the Frank Laboratory of Neutron Physics, Dubna, Russia (Ullemeyer *et al.*, 1998); and NOMAD at the Oak Ridge National Laboratory Spallation Neutron Source, TN, USA (Peterson *et al.*, 2021). Each beamline has specific instrument coordinate conventions, and users at these facilities employ a variety of software packages to analyze diffraction data. During an experiment, the sample frame must be known in the instrument coordinate system. This is often achieved by aligning a feature, such as a cylinder axis or an arrow on the sample, with part of the sample holder or instrument. This orientation and any rotations of the sample during data collection also need to be documented, for example, in a data collection file.

After collection, diffraction data are analyzed using diffraction analysis software such as *MAUD* (*Materials Analysis Using Diffraction*) (Lutterotti *et al.*, 1997; Lutterotti, 2010), *FullProf* (Rodríguez-Carvajal, 2001), *TOPAS* (Coelho, 2018), *Jade* (Jennings, 2021), *GSAS* (Larson & Von Dreele, 1994) or *GSAS-2* (Toby & Von Dreele, 2013). Diffraction analysis is conducted with various degrees of sophistication from simple preferred orientation correction to full texture

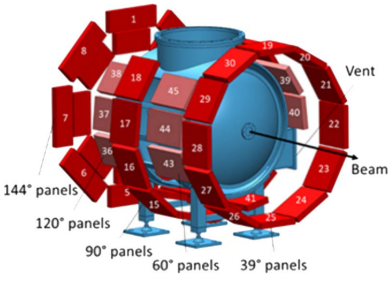

analysis. These software programs typically retrieve the detector coordinates from instrument parameter files [*e.g.* pairs of polar coordinates consisting of the diffraction angle (Bragg angle 2ϑ between the incident beam and diffracted beam) and the azimuth angle (defining angular offset from the diffraction plane) for *GSAS*-format instrument parameter files], which poses a potential source of error if a thorough evaluation of reference frames and software integration has not been carried out for a particular instrument. The intent of the procedures described here is to provide practical guidance for validating texture measurements and to apply the procedures to an experimental dataset from HIPPO.

The above-mentioned software packages can determine texture and other material parameters (*e.g.* phase fractions, lattice parameters, residual stress) using the Rietveld refinement process which models diffraction intensity (Rietveld, 1969; McCusker *et al.*, 1999). Texture interpretation software such as *BEARTEX* (Wenk *et al.*, 1998) and *MTEX* (Bachmann *et al.*, 2010) have their own convention for or allow the user to specify their own coordinate systems, and these systems need to be taken into account when further processing the texture.

It is critical to keep track of the different coordinate systems and rotation axes involved with a particular instrument to ensure the relationship between crystal orientation and the sample coordinate system is preserved through data collection, Rietveld analysis and texture interpretation. Even if documentation of coordinate system definitions for the instrument and analysis software exists, it is still valuable to verify these because changes to software or hardware (*e.g.* a new rotation stage with a different direction of the rotation motion) can violate previous definitions and go unnoticed. For example, the definition of the instrument coordinate system ($\mathbf{X}_i\mathbf{Y}_i\mathbf{Z}_i$) for neutron texture analysis with HIPPO defines the $\mathbf{Y}_i$ axis vertically up (Wenk *et al.*, 2010; Matthies *et al.*, 2005, pp. 463–464, Figs. 1 and 3), whereas for a synchrotron texture instrument at the Swiss Light Source the $\mathbf{Y}_i$ axis is defined vertically down (Grässlin *et al.*, 2013, p. 174, Fig. 1). Though these two definitions are equivalent and the choice depends on the instrument, the definition needs to be known when relating a sample orientation or rotation to the given instrument coordinate system. An example of dissimilar coordinate systems for HIPPO was found by Takajo & Vogel (2018, p. 896, Fig. 1), who determined pole figure coverage in a separate software from *MAUD* and adopted a different coordinate system. This example of multiple reported coordinate systems for a given instrument underlines the need to understand coordinate system definitions in the software packages used.

In addition to the definition of the instrument coordinate system, the definition of the rotations (clockwise or counter-clockwise) around these axes and the angle conventions used to define detector locations need to be understood and verified: in *MAUD* the χ_s and ϕ_s rotations around the $\mathbf{X}_i$ and $\mathbf{Z}_i$ axes, respectively, are defined as counter-clockwise rotations, whereas the ω_s rotation and the 2ϑ diffraction angle around the $\mathbf{Y}_i$ axis are defined as clockwise rotations (Grässlin *et al.*, 2013). Wenk *et al.* (2010) incorrectly reported that all rotations in *MAUD* are defined as clockwise rotations. Careful analysis of the coordinate systems and rotation axes involved in HIPPO experiments during the work reported here has led to the identification of a previously unnoticed inconsistency in *MAUD* related to the detector azimuthal angle η, which has been corrected since *MAUD* version 2.996. This again underlines the need for documentation and verification of these definitions, as described here.

In this paper, we provide a process for the verification of the coordinate systems involved in a diffraction texture experiment with the HIPPO TOF diffractometer and show the steps necessary to verify that the correct coordinate system is maintained from data collection to the texture analysis of the final orientation distribution data and plotted result. For this process, a quartz crystal was chosen due to the correlation of the physical shape of the sample (*i.e.* pyramidal and rhombohedral crystal faces representing the trigonal crystal structure) with the orientation of the sample as it is mounted in the instrument. The trigonal crystal structure of quartz is advantageous over a cubic material as it breaks the symmetry of the orthogonal coordinate axes of instrument and sample coordinate systems [see the aforementioned references on texture analysis as well as Matthies *et al.* (1988, pp. 463–464) for a discussion of coordinate systems used in texture analysis]. Furthermore, millimetre- to centimetre-sized quartz single crystals are readily available, which is typically not the case for other lower-symmetry crystals (monoclinic or triclinic). Symmetrical 120° rotation elements of triclinic crystals are unlikely to be confused with errors in texture representation using established software (typically instrument definitions differ by 90 or 180° rotations). Quartz therefore provides a good test for the verification of coordinate systems involved in texture analysis.

The Rietveld software *MAUD* (Lutterotti, 2010), similarly to other Rietveld codes such as *GSAS* and *GSAS-2* (Von Dreele, 1997), allows texture analysis from diffraction data originating from several instrument types. *MAUD* can process both neutron (TOF and monochromatic) and X-ray (classical goniometers and synchrotron diffraction images) data. We note that other Rietveld codes (*e.g. GSAS-2*) have similar features to *MAUD* for plotting pole figure coverage resulting from a given experiment, making the methods described here non-specific to the *MAUD* software alone. *MAUD* was used for the analysis of quartz instead of *GSAS*/*GSAS-2* because the spherical harmonic texture model employed by *GSAS* is not suitable for sharp textures like those produced by a single-crystal sample. While *GSAS* and *GSAS-2* use spherical harmonics functions to describe the orientation distribution function (ODF), which interpolate between weights for orientations with smooth functions, *MAUD* describes the ODF with the E-WIMV method, which is a discrete method, allowing the user to assign weights to orientations in Euler space on, for example, a 1° grid completely independent from each other. Similarly to describing a delta function with a Fourier synthesis, the spherical harmonics description of an ODF for a single crystal will result in many oscillatory artifacts. However, a 1° resolution E-WIMV description will

assign weights to only one or two grid points in Euler space, thus describing an ODF much more accurately.

2. Coordinate systems

In crystallographic texture analysis, the orientation of a crystal is described relative to the sample frame of references by a set of three Euler angles (Bunge & Roberts, 1969; Kocks *et al.*, 1998; Wenk & Van Houtte, 2004) which are three rotations that bring the two coordinate systems to coincidence. Several coordinate systems must be considered to correctly obtain the set of Euler angles: consider a sample with its own coordinate system ($\mathbf{X}_s\mathbf{Y}_s\mathbf{Z}_s$) mounted within an instrument, again with its own coordinate system ($\mathbf{X}_i\mathbf{Y}_i\mathbf{Z}_i$). In general, for example, in Bragg–Brentano type diffractometers where incident and diffracted beams define the diffraction, typical axes for the instrument coordinate system consider the beam direction, its orthogonal direction in the diffraction plane and the normal to the diffraction plane defining a Cartesian coordinate system. In *MAUD* specifically, the $\mathbf{X}_i$ axis is defined along the beam direction, pointing from the source towards the sample, the $\mathbf{Z}_i$ axis lies in the diffraction plane pointing at $2\vartheta = +90^\circ$ and $\mathbf{Y}_i$ is defined such that ($\mathbf{X}_i\mathbf{Y}_i\mathbf{Z}_i$) is a right-handed orthogonal coordinate system (in parentheses bold denotes an orthogonal set of vectors). Fig. 1 below shows the instrument coordinate system for HIPPO.

For instruments without a natural diffraction plane, *i.e.* in instruments where multiple diffracted beams are detected such as HIPPO or a 2D detector system at an X-ray beamline, the diffraction plane can be arbitrarily chosen, and a convenient choice is the plane such that the Bragg angle 2ϑ and ω sample rotation axes are coaxial [the horizontal plane in HIPPO or a plane correlated to the polarization plane (the plane in which linearly polarized X-rays oscillate) in a synchrotron beamline]. The former choice is a convention connecting the detector geometry with the texture goniometer. These considerations lead to the choices of instrument coordinate systems as defined by Grässlin *et al.* (2013) for a synchrotron diffraction instrument and Matthies *et al.* (2005) for TOF neutron diffraction.

The Cartesian sample coordinate system ($\mathbf{X}_s\mathbf{Y}_s\mathbf{Z}_s$) is typically defined by processing (*e.g.* rolling direction, normal direction and transverse direction for rolled metal samples) or sample geometry (*e.g.* axial direction and two radial directions for cylindrical samples) (Chateigner *et al.*, 2019; Gilmore *et al.*, 2019). For texture analysis, a Cartesian crystal coordinate system ($\mathbf{X}_c\mathbf{Y}_c\mathbf{Z}_c$) is chosen which may differ from the coordinate system of the crystallographic unit cell in which the atomic positions are defined. Definitions that *MAUD* follows for the Cartesian crystal coordinate systems for different crystal symmetries are given in Table S1 of the supporting information, which has been adapted from Table 5.1 of Matthies *et al.* (1987). In cubic, tetragonal and orthorhombic crystal systems the unit-cell axes **a**, **b** and **c** correspond to ($\mathbf{X}_c\mathbf{Y}_c\mathbf{Z}_c$). In the case of a hexagonal or trigonal (in the hexagonal setting) crystal lattice system, the convention prescribed in Table S1 is $\mathbf{X}_c \parallel \mathbf{a}$, $\mathbf{Y}_c = \mathbf{Z}_c\mathbf{X}_c$, $\mathbf{Z}_c \parallel \mathbf{c}$ (where **a** and **c** are the corresponding unit-cell vectors in the hexagonal unit cell, see Fig. 2). For other space groups we refer the reader to Table S1 or Table 5.1 of Matthies *et al.* (1987).

Euler angle rotations are used to relate the sample to the crystal coordinate system, thus allowing the user to describe any crystal orientation in the sample coordinate system [see Matthies *et al.* (1987) for the different definitions of Euler angles such as Bunge or Roe/Matthies]. In *MAUD*, the Euler angles are defined by the Roe/Matthies convention. To

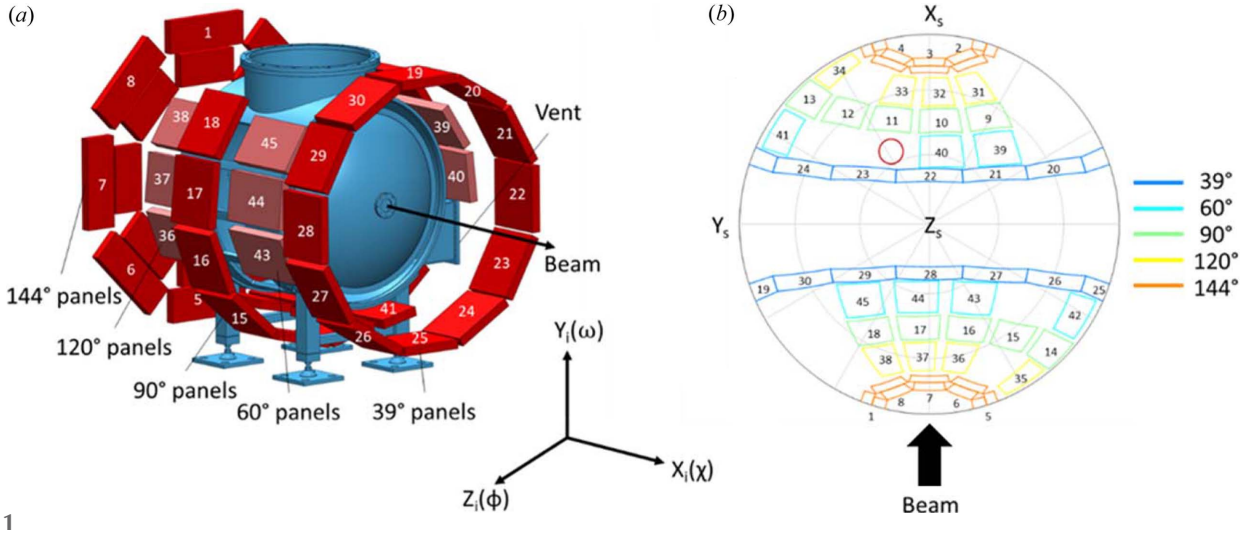

Figure 1
(*a*) Schematic of the HIPPO instrument at LANSCE. Note the location of the flange of the sample chamber (top) and the vent (right side in the 60° detector ring) where the neutron detectors are missing. (*b*) Equal area projection of HIPPO detectors onto a generic (*hkl* independent) pole figure. Differently from constant-wavelength texture measurements, the pole figure coverage in a neutron TOF experiment is the same for all (*hkl*). Note the resulting large gap in the detector coverage from the HIPPO sample chamber flange and the missing detector panel (red circle) due to the vacuum vent which would mirror panel No. 43 with respect to a vertical mirror plane. The correlation of the pole figure coverage plot at $\omega_s = 0^\circ$, $\chi_s = 0^\circ$, $\varphi_s = 0$ with the instrument detector layout is shown in more detail in Fig. 4.

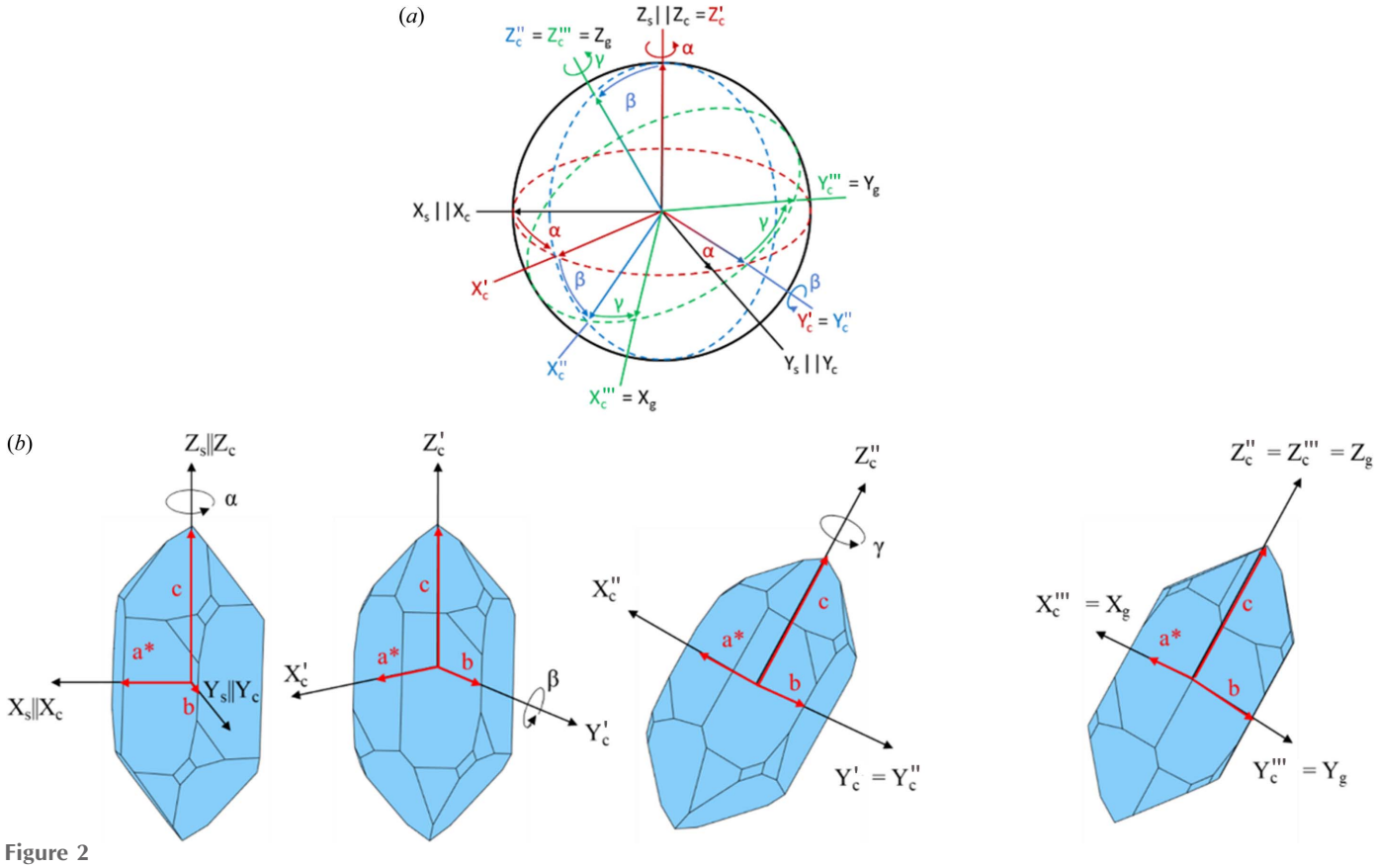

Figure 2
(*a*) Stereographic projection showing the Matthies–Euler convention relationship between the sample ($\mathbf{X}_s\mathbf{Y}_s\mathbf{Z}_s$), crystal coordinates ($\mathbf{X}_c\mathbf{Y}_c\mathbf{Z}_c$) and coordinates at a given orientation ($\mathbf{X}_g\mathbf{Y}_g\mathbf{Z}_g$). (*b*) Illustration of crystal coordinate axes $\mathbf{X}_c\mathbf{Y}_c\mathbf{Z}_c$ in quartz shown aligned with the axes of the sample coordinate system $\mathbf{X}_s\mathbf{Y}_s\mathbf{Z}_s$ following the rotations in (*a*) to give the final orientation ($\mathbf{X}_g\mathbf{Y}_g\mathbf{Z}_g$). Note that, to describe the trigonal crystal unit-cell axes (red) with the orthogonal crystal coordinate system, one crystal axis is a reciprocal axis. Orientations here are defined by Matthies–Euler rotations α, β and γ around $\mathbf{Z}_c$, $\mathbf{Y}'_c$ and $\mathbf{Z}''_c$, respectively (prime, double- and triple-prime superscripts indicate the rotated axes), to arrive at the final crystal orientation in ($\mathbf{X}_g\mathbf{Y}_g\mathbf{Z}_g$).

visualize this definition, we show the reorientation of a quartz crystal in the sample coordinate system to an orientation $g = (\alpha, \beta, \gamma)$ using the Matthies convention in Fig. 2(*b*).

Diffraction analysis programs [*e.g. GSAS-2* (Toby & Von Dreele, 2013) or *MAUD* (Lutterotti, 2010)] as well as texture analysis software [*e.g. MTEX* (Bachmann *et al.*, 2010) or *BEARTEX* (Wenk *et al.*, 1998)] may use their own conventions to define coordinate systems and these must be taken into account. Definitions for the orientations of crystals, as used to describe the orientation distribution or 'texture', use mostly the Euler angle system in either the Bunge or the Matthies convention (Bunge, 1969; Kocks *et al.*, 1998). Compatible data formats need to be adopted to export and import ODFs and pole figures between different software in addition to following the same Euler angle convention. For example, the coordinate convention in *MTEX* is user defined and fully general, but a setting in agreement with the convention used in the software from which data is imported (*e.g. MAUD*) has to be chosen. The user must be aware of the available file formats (*e.g. BEARTEX* or *popLA* file formats for pole figures or ODFs) of the exporting software to correctly import into texture-processing codes such as *MTEX*. The agreement between coordinate systems is of paramount importance, for example, when deriving bulk properties of a rolled polycrystalline metal relative to the rolling geometry (Wenk & Van Houtte, 2004) and when analyzing tensor quantities of low-symmetry crystals.

3. Verifying coordinate systems of instrument and analysis software

To illustrate the instrument coordinate system, the detector layout of the HIPPO diffractometer is described. HIPPO is a TOF neutron diffractometer introduced in 2002 (Wenk *et al.*, 2003; Takajo & Vogel, 2018) and since then modified from the original 10, 20, 39, 90 and 144° detector rings to a configuration with five detector rings at nominal diffraction angles of 39, 60, 90, 120 and 144° from the incident beam direction [Fig. 1(*a*)]. The instrument symmetry around the incident beam is broken by the absence of detector panels at the top of the 60, 90 and 120° rings, corresponding to the location of the instrument door for access to the sample chamber from the top. In addition, the symmetry is broken by an absent detector panel in the 60° ring corresponding to the location of a vacuum vent for the sample chamber as shown in Fig. 1(*a*). The missing detector panels can be noticed in the generated pole figure

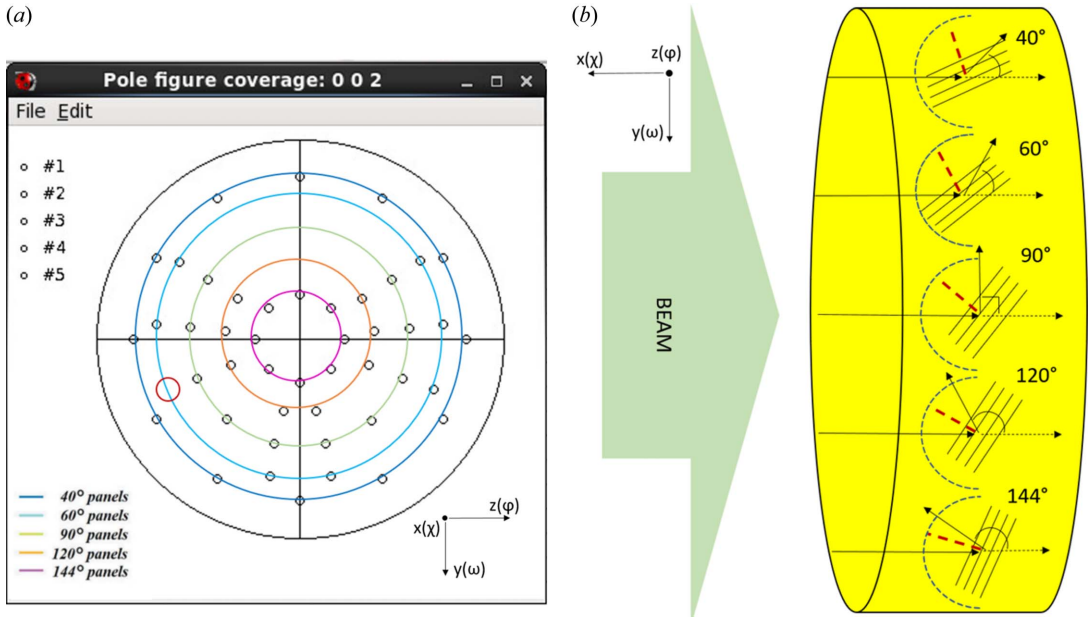

Figure 3
(*a*) The diffraction vectors corresponding to the detector panels on the five detector rings on HIPPO are mapped on the pole figure at sample rotation $\omega_s = 90°$, $\chi_s = -90°$, $\phi_s = 0°$ viewed along the beam ($+\mathbf{X}_i$ direction). Note the missing detectors corresponding to locations of the HIPPO door (large empty area in the upper half) and vacuum vent (red circle in bottom left quadrant). (*b*) Diagram showing vectors of diffracted neutrons pointing towards the five different detector rings on HIPPO (with the nominal diffraction angles of the rings shown) with the corresponding diffraction vectors (bisecting incident beam vector and the vector representing diffracted neutrons). Note that the three-dimensional arrangement of the HIPPO detector panels results in rings of diffraction vectors around the direction of the incident beam.

coverage plots [Fig. 1(*b*) and Fig. 3(*a*)]. The projection in Fig. 1(*b*) shows the geometry of the detector panels rather than just points for each panel as in the pole figure plots produced by *MAUD* [*e.g.* Fig. 3(*a*)]. The coverage area with detectors for this configuration is 22.4% of 4π steradians. We note that for the analysis in *MAUD* the physical detector panel areas are treated as single points (defined by the polar detector coordinates as shown in the *MAUD* pole figure coverage plots). The data reduction, integrating the detected intensity of each detector panel into a single histogram for the Rietveld analysis, also manifests this approximation. Although the diffracted intensity of a single crystal is spatially confined to a small spot on the detector panel, it can be shown that, for example, a 1° rotation of the crystal in HIPPO results in a readily measurable change of the diffraction signal and therefore the entire instrument is sensitive to small changes in orientation. A study of the effect of this approximation on the texture analysis is still ongoing and is the subject of a future publication.

On HIPPO, the sample is typically rotated by 0, 67.5 and 90° around the vertical axis to improve the pole figure coverage to 51% (Takajo & Vogel, 2018). The fact that the detector coverage is asymmetrical is critical for ensuring the correct preservation of coordinate systems because in the case of a symmetrical detector arrangement sample rotations may result in identical pole figure coverages. This in turn may lead to undetected problems with the coordinate system definitions. In other words, the broken symmetry of the detector arrangement and therefore the asymmetric pole figure coverage allows the pole figure coverage to be unambiguously related to the instrument layout.

Texture analysis from HIPPO (and other instruments) diffraction data, *i.e.* the calculation of the ODF from measured diffraction peak intensities, is routinely done using *MAUD* (Wenk *et al.*, 2003, 2010; Vogel *et al.*, 2004; Matthies *et al.*, 2005). *MAUD* pole figure coverage plots show the diffraction vector for each detector projected onto a pole figure [in *MAUD*: 'Graphic' – 'Texture plot' – 'Pole figure coverage', Fig. 3(*a*); see also Takajo & Vogel (2018)]. Pole figures are defined in the sample coordinate system, whereas the diffraction vectors, based on the incident beam and detector location, are defined in the instrument coordinate system. In *MAUD* pole figures, the $\mathbf{Z}_s$ axis is always normal out of the pole figure plane with $\mathbf{X}_s$ pointing to the top (north) and $\mathbf{Y}_s$ to the left (west) of the pole figure. The orientation of the sample coordinate system relative to the instrument coordinate system, *i.e.* the viewpoint of the pole figure with respect to the sample, is controlled by the angles ω_s, χ_s and ϕ_s in the sample position parameters of *MAUD*. Thus, these angles can be used to align a direction on the physical sample in the instrument, *e.g.* a rolling direction, with the sample coordinate system of *MAUD*, such that the rolling direction is pointing north in the resulting pole figure. *MAUD* preferences that influence how the coordinate system is defined are provided in Table S2. Using *MAUD*, the ring-based detector layout of HIPPO is best visualized in pole figure coverage plots by rotating the sample coordinate system such that the detectors of each ring lie on a corresponding circle that is not broken by the horizon of the pole figure [$\omega_s = 90°$, $\chi_s = -90°$, $\phi_s = 0°$ in 'Sample' – 'Sample position' dialog in *MAUD*] as shown in Fig. 3(*a*). In this projection, viewing the pole figure coverage along the beam direction does not require projection for any detector

across the pole figure horizon. Detector locations on the same detector ring are identified as colored rings in Fig. 3(*a*). Note that in this orientation the missing detector panels corresponding to the door of HIPPO are at the top of the figure and the missing 60° detector panel associated with the vacuum vent [red circle in Fig. 3(*a*)] is at the bottom left of the pole figure. For additional illustration, we show a side view of the HIPPO instrument and the neutron beam interacting with different lattice plane orientations in a sample in Fig. 3(*b*). The locations of the lattice plane normals, poles or diffraction vectors corresponding to the 39, 60, 90, 120 and 144° detectors, denoted by the colored circles in Fig. 3(*a*), are represented by their diffraction angles or scattering vectors (red dashed lines) in Fig. 3(*b*).

Plots projecting the diffraction vectors for an asymmetric detector arrangement, such as the pole figure coverage plots, can be used to verify the instrument coordinate system with the detector orientation being used in the diffraction analysis software. Fig. 4 was generated by plotting pole figure coverage for HIPPO for sample goniometer rotations of −90, 0 and 90° around the three axes $\mathbf{X}_i(\chi_s)$, $\mathbf{Y}_i(\omega_s)$ and $\mathbf{Z}_i(\varphi_s)$ in the *MAUD* instrument coordinate system (done in *MAUD* by changing the values in the sample position window 'Sample' – 'Sample position'). These plots are used to identify the orientation of the instrument coordinate system in *MAUD* by following the transformations of the missing detectors (door and vent) in the pole figure coverage plots for each rotation. The rotation axes are given in the bottom right of each sub-figure in Fig. 4. For additional visualization, the orientation of the HIPPO instrument and a HIPPO sample holder corresponding to the orientation of the sample coordinate system (as defined by the sample goniometer angles shown in each sub-panel) are added. The notch in the sample holder enables the correlation of the sample when mounted with the sample orientation during the measurement. As mentioned before, in *MAUD* the rotations for χ and ϕ, around $\mathbf{X}_i$ and $\mathbf{Z}_i$, respectively, are defined counter-clockwise, whereas the ω rotation around $\mathbf{Y}_i$ is defined as a clockwise rotation. Clockwise and counter-clockwise rotations are defined around the positive vector direction.

The coordinates from *MAUD* in Fig. 4 differ from the conventions that have been published in the literature (Wenk *et al.*, 2010, p. 285, Fig. 2; Matthies *et al.*, 2005, pp. 463–464, Figs. 1 and 3) due to errors in the way η was defined in previous versions of *MAUD* that have been corrected in *MAUD* version 2.996. Prior to this version, instruments utilizing η to define detector locations resulted in pole figures with $\mathbf{X}_s$ pointing south and $\mathbf{Y}_s$ pointing east. After this

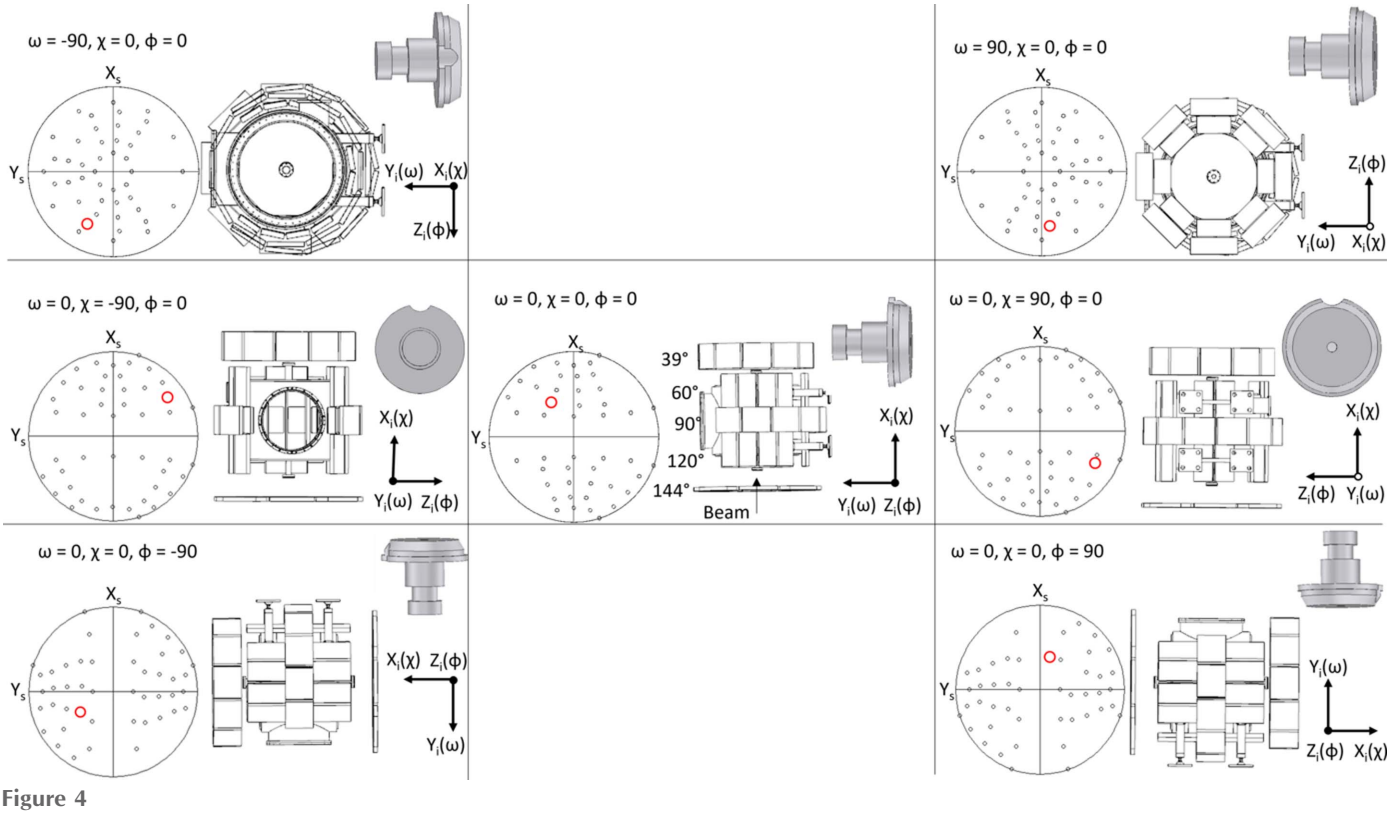

Figure 4
The sample rotation angles ω_s, χ_s and φ_s change the perspective on the pole figure coverage (and fixed sample inside the instrument). The scattering vectors in the pole figure coverage plot, representing the diffraction vectors for each detector panel, should rotate in the opposite sense of the sample rotation angles. With this understanding we can track the asymmetric features in *MAUD* (vent, indicated by red circle, and door, the large gap in the coverage) and verify that the coordinate system transformation calculated by *MAUD* agrees with the definition of rotations (see text). The coverage plots and corresponding viewpoints of the HIPPO instrument and sample holder are shown for changing ω_s, χ_s and φ_s individually as indicated. The sample coordinate system, in which the pole figures are defined, remains constant as defined in the text. Note that the diffraction vectors in the southern hemisphere are plotted as antipodes.

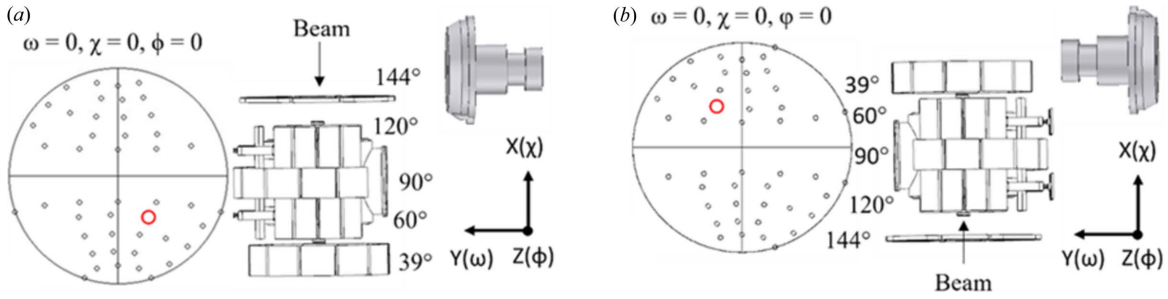

Figure 5
Comparison of pole figure coverage plots for HIPPO (*a*) before and (*b*) after the bug related to η was fixed in *MAUD* version 2.996.

correction, pole figures now follow the convention that $\mathbf{X}_s$ points north and $\mathbf{Y}_s$ points west. A comparison between the pole figure coverage plots before and after this correction is shown in Fig. 5.

4. Experimental verification for texture analysis

To verify that the results of the texture analysis are correct, a sample with a known asymmetric orientation distribution needs to be measured. A non-cubic single crystal, allowing the user to relate the crystal orientation to the crystal faces, is a suitable sample for such a test. Here, the 'texture' of a natural α-quartz crystal is analyzed using *MAUD* version 2.996 to demonstrate the verification process. The α-quartz crystal structure is trigonal with the space group $P3_121$ (space group No. 152 in *International Tables for Crystallography*). The quartz crystallographic data file (CIF) from Le Page & Donnay (1976) was used in this study. Note that the difference between left and right quartz cannot be resolved with neutrons. The hexagonal lattice geometry is expressed in diffraction peak positions whereas the trigonal symmetry is observed in peak intensities. Fig. 6(*a*) shows the crystal mounted on a HIPPO sample holder and Fig. 6(*b*) shows a close-up of the crystal with {10$\bar{1}$0} planes and the **c** axis of the crystal highlighted, allowing the user to identify the crystal orientation relative to the sample holder. Fig. 6(*b*) shows that the **c** axis of the crystal is tilted approximately 25° off the sample holder axis (**Z**). The normal of the prism plane {10$\bar{1}$0} is perpendicular to the **c** axis with poles of one of the three plane pairs approximately perpendicular to the viewing direction.

Data were collected for 2 min per rotation at rotation angles of $\omega_i = 0$, 67.5 and 90° with the HIPPO robotic sample changer (Losko *et al.*, 2014). The steps of the Rietveld refinement are described in the supporting information in some detail. Here we give a brief summary. For the *MAUD* refinement, 3 × 45 = 135 diffraction patterns were used following the following strategy: (1) The background was refined using three polynomial parameters for each detector at each orientation. The HIPPO incident intensity parameter was set to a value of 0.0007 to adjust the intensities of the fit to the approximate order of magnitude. Scale factors were also refined in this step. (2) In the second step of the refinement, all background parameters were fitted, an arbitrary texture was applied and DIFC/shift parameters were fitted (defining the distance

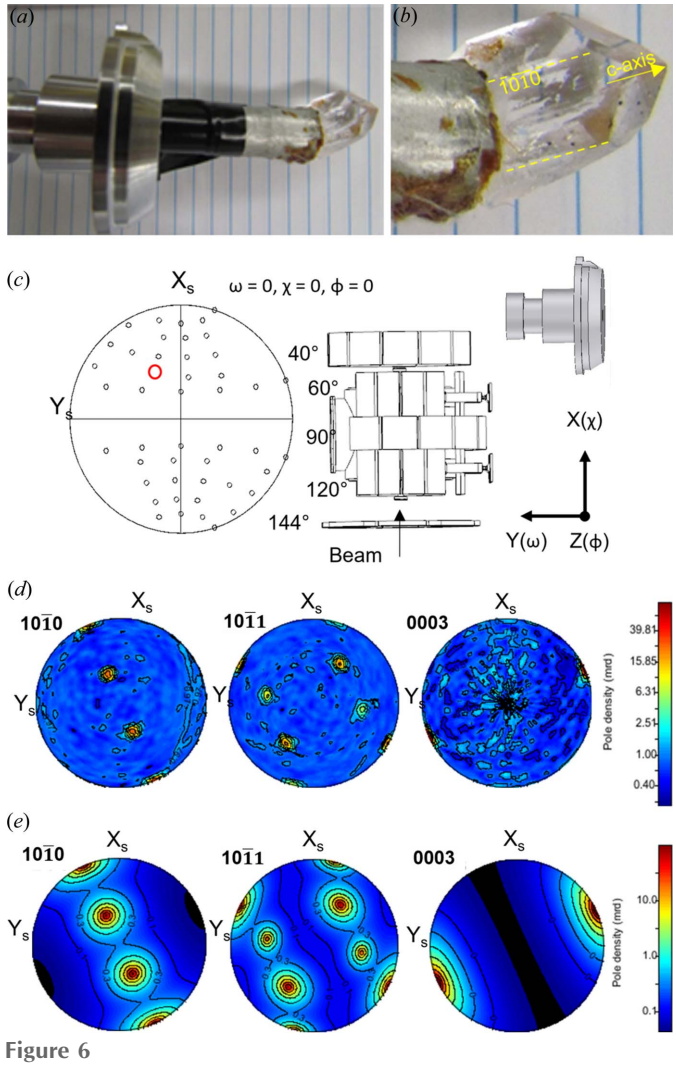

Figure 6
(*a*) Quartz crystal mounted on a HIPPO sample holder with a prismatic (10$\bar{1}$0) face normal pointing to the notch of the sample holder. The sample holder is rotated by ∼30° around the sample holder axis such that the notch becomes visible to the viewer. (*b*) Close-up of the quartz crystal in this orientation, highlighting the (10$\bar{1}$0) faces and the **c** axis of the crystal, which is misaligned by ∼25° with respect to the sample holder axis. (*c*) *MAUD* pole figure coverage, instrument and sample holder orientation corresponding to the orientation in the photograph (except for the ∼30° rotation in the photograph). (*d*) (10$\bar{1}$0), (10$\bar{1}$1) and (0003) pole figures extracted from the diffraction data using *MAUD*. (*e*) Uncommon analysis using standard function main crystal orientations observed in (*d*) used to investigate twinning in the (10$\bar{1}$1) pole figure. An imperceptible improvement in the Rietveld refinement fit when including a twin with 60° offset indicates that the twin may be an artifact of insufficient pole coverage for single-crystal texture analysis.

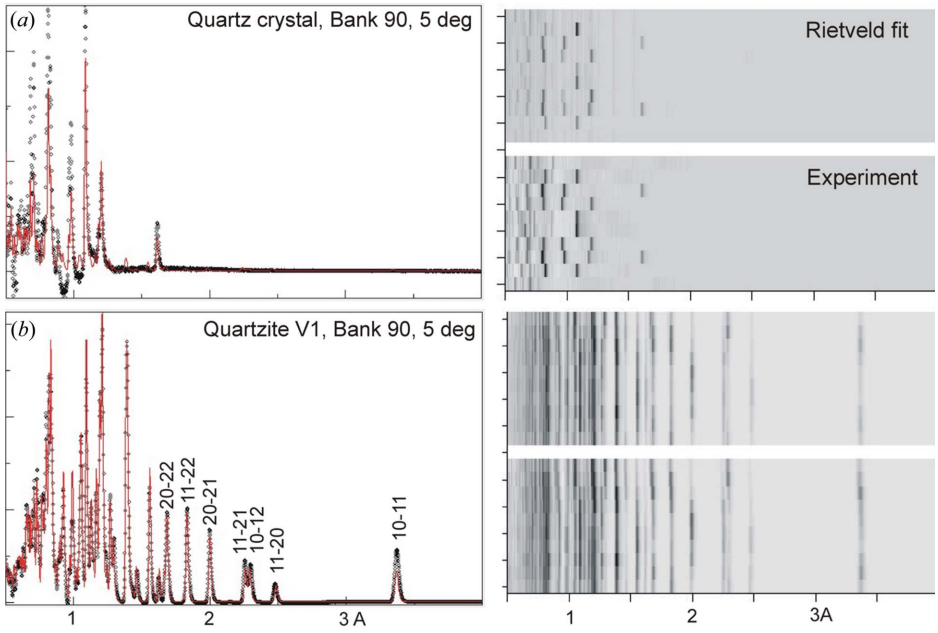

Figure 7
(*a*) HIPPO analysis for the single quartz crystal used in this study. (*b*) HIPPO analysis of a naturally deformed quartzite pebble from northern Spain (Chen *et al.*, 2012). Left: sum of spectra for detector bank 90. Red lines are the Rietveld fit. Right: stack of individual spectra. Bottom: experiment. Top: Rietveld fit. The excellent agreement in (*b*) suggests a reliable analysis.

between sample and detectors). (3) In the final step, the E-WIMV texture with a resolution of 1 and 5° was explored, and we show details for the 5° refinement. The data range considered for this refinement was 0.5–4.0 Å. The pole figure coverage, position of the sample holder and experimental view of the HIPPO instrument in *MAUD* at the sample rotation angles $\omega_s = 0°$, $\chi_s = 0°$, $\phi_s = 0°$ are shown in Fig. 6(*c*). Pole figures of the refined crystal orientation are plotted in Fig. 6(*d*).

5. Quality of Rietveld fit and role of diffraction intensities

Fig. 6(*d*) demonstrates a good fit for the hexagonal lattice [(0003) and (10$\bar{1}$0)] which has been used to define the coordinate system. Curiously, the (10$\bar{1}$1) pole figure suggests that this quartz is not a trigonal single crystal but a composite of two crystals rotated 60° around the common **c** axis. The resolution of the **c** and **a** axis positions depends on diffraction peak positions, but the resolution of trigonal symmetry depends on the diffraction intensities (Chen *et al.*, 2012). This could be due to Dauphiné twinning or an artifact in the HIPPO experiment.

The single-crystal spectra in this study, shown in Fig. 7(*a*), do not show good agreement. The black measured data and the red calculated spectrum for the quartz single crystal show overall agreement in peak positions but the intensities are poorly modeled. This is highlighted in 'Plot 2D' of individual detectors on a bank. The peak positions are reliable, but the intensities vary widely. Moreover, the agreement is worse for some rotations of the sample (ω). Generally, for polycrystalline samples there is good agreement between measured and calculated diffraction spectra, as illustrated in Fig. 7(*b*) for quartzite measured on HIPPO with very similar experimental configurations. The averaged diffraction spectrum (left) and the stack of individual diffraction spectra (right) show excellent agreement between peak positions as well as peak intensities.

We attribute the poor fit quality to the geometry of the HIPPO diffractometer which was designed to measure not single crystals but powders of polycrystalline materials. In fact, the detectors shown in Fig. 2 are not uniform surfaces like X-ray area detectors used in synchrotrons but are composed of many individual tubes ∼1 cm in diameter and ∼35 cm long. For a powder the diffraction intensity covers a broad area that is averaged, but a single crystal produces sharp spots that may

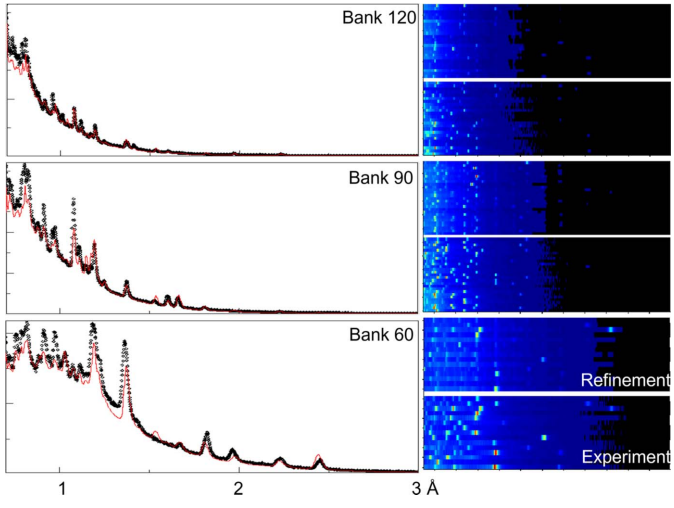

Figure 8
Rietveld fits of the HIPPO analysis of the quartz single crystal described in this paper. Diffraction peaks occur at the correct positions, but the intensities are erratic, which can be attributed to the instrumental limitations.

fall between tubes, or individual tubes may malfunction. Thus, intensity recorded by the whole detector will be subject to spatially varying detector efficiency when measuring single crystals which is much less problematic when measuring polycrystalline samples. We suspect that this is the reason for the poor resolution of trigonal symmetry in quartz which relies on peak intensities (Chen *et al.*, 2012). *MAUD* tries to compensate for these intensity problems by refining Dauphiné twins which are at the same diffraction angles, but this does not resolve the intensity problem as shown in Figs. 7(*a*) and 8. The Dauphiné twinning suggested in the $(10\bar{1}1)$ pole figure in Fig. 6(*d*) is therefore likely to be an artifact.

6. Consistent coordinate system representation in texture analysis software

The next step in analyzing the texture of a material often involves importing data into texture analysis software such as *MTEX* (Bachmann *et al.*, 2010) or *BEARTEX* (Wenk *et al.*, 1998). Obtaining the ODF in texture analysis software can be done either by importing reconstructed pole figure data and recalculating the ODF or by directly importing the ODF. ODF reconstruction from pole figure data is typically done in *MTEX*, whereas direct ODF import is done in *BEARTEX*. *MTEX* can also import ODFs; however, the authors noticed that the cell representation used in *MAUD* and automatic rebinning to a 5° cell to standardize ODF export result in more artifacts compared with using pole figures. Calculation of ODFs from pole figures has one downside in that, if the crystal axis definition is not consistent with *MAUD*, a different ODF will be refined from the pole figures. This is not an obvious mistake since the pole figures in *MTEX*, for example, can still look the same as those in *MAUD*. In addition to exporting reconstructed pole figures, *MAUD* can export the extracted texture factors for each diffraction vector in `.apf` phase files. These files are the data for the experimental pole figures in *MAUD* and can be directly fitted or visualized in *MTEX*.

The data for 30 reconstructed pole figures (in 5° intervals for the azimuth and pole distance) were exported from *MAUD*, loaded into *MTEX* using the *MTEX* import wizard and used to reconstruct the ODF in *MTEX* (Rafailov *et al.*, 2020). To preserve the sample coordinate system as defined in *MAUD*, we orient the *MTEX* crystal coordinate system such that $\mathbf{X}_c$ and $\mathbf{Z}_c$ in *MTEX* are parallel to the crystallographic axes **a** and **c** of the quartz crystal, respectively. In *MAUD*, the sample coordinate system, in which the Euler angles to

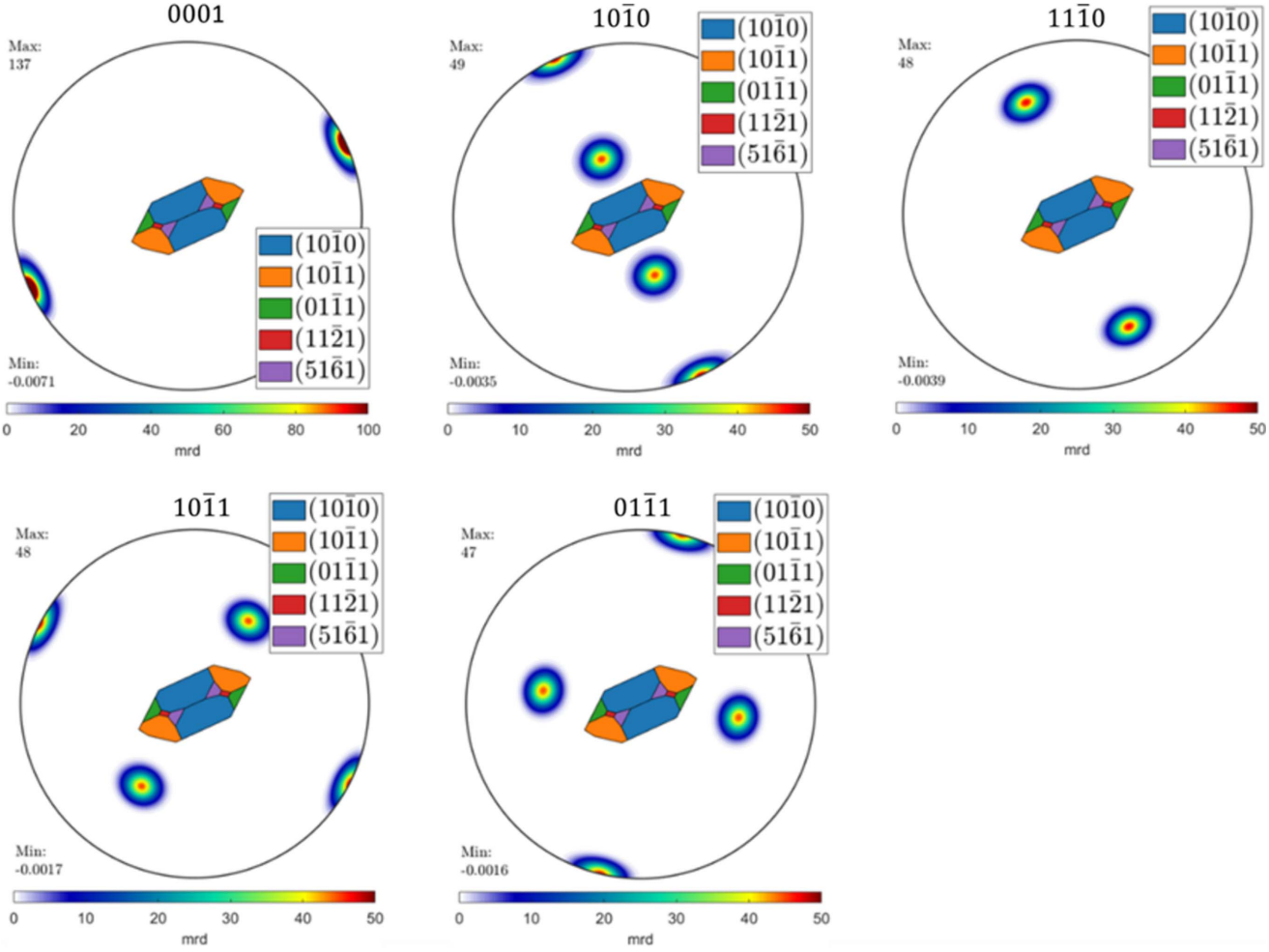

Figure 9
MTEX pole figures showing the crystal orientation of the main quartz texture component (see text for more details).

describe crystal orientations are defined, has $\mathbf{X}_s$ pointing towards 'north' in pole figures, $\mathbf{Y}_s$ towards 'west' and $\mathbf{Z}_s$ out of plane (note that *MAUD* versions prior to 2.996 exported ODF and pole figure data with $\mathbf{X}_s$ pointing towards 'east', $\mathbf{Y}_s$ towards 'south' and $\mathbf{Z}_s$ out of plane, inconsistent with the plotting of pole figures or ODFs in *MAUD*). The *MAUD* output format can now be changed in the 'Analysis Preferences' using the field option 'plot.NWSE' (correct formats for HIPPO data are 'N' and 'E' when outputting to *MTEX* and *BEARTEX*, respectively). To reproduce this plotting convention in *MTEX* a right-handed frame should be set in *MTEX* with the 'xAxisDirection' to be 'north' and the 'zAxisDirection' to be 'outOfPlane'. In Fig. 9, the (0001), $(10\bar{1}0)$, $(11\bar{2}0)$, $(10\bar{1}1)$ and $(01\bar{1}1)$ pole figures are plotted, showing the trigonal symmetry of the crystal and orientation of the major texture component. This visualization of the crystal is an important verification that pole figure or ODF data are properly exchanged between *MAUD* and *MTEX*. To illustrate the importance of verifying the proper exchange of pole figure or ODF data between *MAUD* and *MTEX*, we provide examples of a correct and an incorrect import. For this, an ODF consisting of a single orientation described by a spherical component in *MAUD* was defined. Fig. 10 shows the (002) pole figure generated in *MTEX* after importing *MAUD*-calculated pole figures into *MTEX* using the correct *MTEX* coordinate system definition (**x** – north, **z** – out of plane) and the incorrect definition (**x** – east, **z** – out of plane, as required for versions of *MAUD* prior to version 2.995). Clearly the resulting crystal orientations in *MTEX* are different.

For *BEARTEX*, the ODF is exported in ASCII format from *MAUD* with 5° cells regardless of the ODF resolution used during refinement [`Phases/Advanced models/Texture: E-WIMV/Options: Export ODF formatted (text) for Beartex`]. Using *BEARTEX*, the *MAUD* output (`fn.mod`) is converted to binary (`Convert: CMAU`, `fn.yom`) and if necessary, data can be smoothed in `Process: SMOO`. Then pole figures are calculated (`Process: PCAL`, `fn.xpo`) and plotted with various options to comply with publication formats (`Display: PING`).

MTEX and *BEARTEX* allow the user to generate publication-quality pole figures and enable texture analysis to determine volume fractions of texture components and calculate anisotropic physical properties. Comparing *MTEX* and *BEARTEX* poles figures with those from *MAUD*

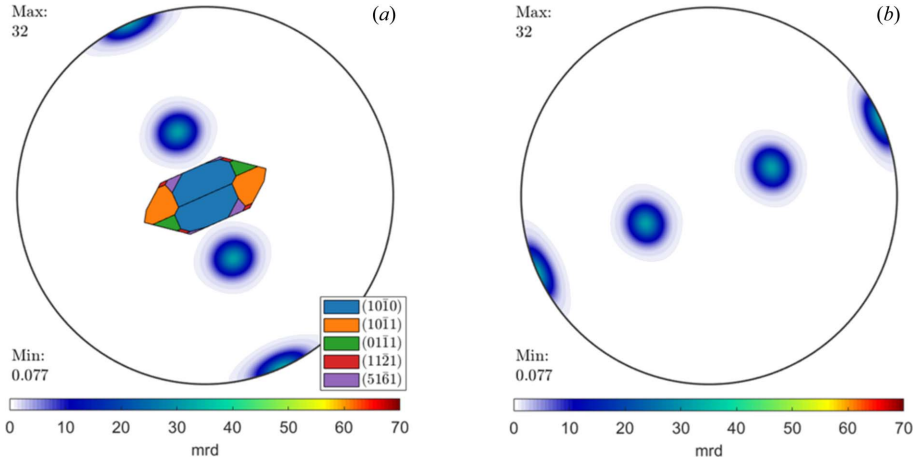

Figure 10
MTEX (002) pole figures computed from the standard function in *MAUD* using (*a*) the correct definition of the *MTEX* plotting convention and (*b*) the incorrect definition of plotting conventions.

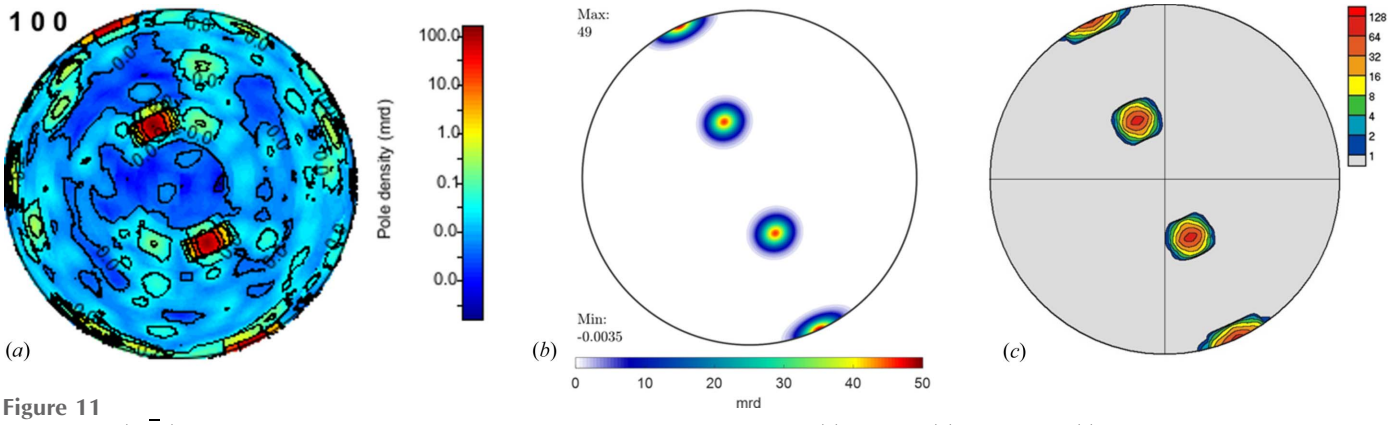

Figure 11
Comparison $(10\bar{1}0)$ pole figures generated from the measured quartz crystal pole figures with (*a*) *MAUD*, (*b*) *MTEX* and (*c*) *BEARTEX* after importing the *MAUD* ODF. The agreement of the pole figures visually and the orientation represented in the pole figures indicates that our coordinate systems are preserved though the different software packages. Plots are equal area projections with the density scale in multiples of random distribution.

[Figs. 11(*a*)–11(*c*)] demonstrates that the correct choices for crystal orientation and plotting conventions were made. The major texture components within a sample can be identified using the 'calcModes' function in *MTEX*. For the quartz single crystal, the texture component that represents the orientation of the crystal is $\alpha = 114.7^\circ$, $\beta = 89.8^\circ$, $\gamma = 120.0^\circ$ in Matthies–Euler angles.

Additional verification that the *MTEX* coordinate system agrees with the *MAUD* coordinate system can be desirable for lower-symmetry materials wherein crystal coordinate system options abound. An example is given by simulating an ODF from one spherical component, specified in *MAUD* by Matthies/Roe–Euler angles. Though this would work for any set of Euler angles, we demonstrate this with Euler angles of a quartz single crystal. From the standard function pole figures can be generated in *MAUD*, exported from *MAUD* and imported into *MTEX* using the same method as previously mentioned. The texture component can then be calculated using the 'calcModes' function and the angles should agree with the Euler angles originally used to create the spherical component if everything is done correctly.

Note that the HIPPO diffractometer and the *MAUD* Rietveld analysis using the E-WIMV algorithm are designed for quantitative texture analysis of polycrystalline materials, not a single crystal. For information about single crystals and their atomic structures, different diffractometers are used and different software packages are applied. HIPPO detectors average over large areas [10–15°, Fig. 1(*b*)], and the EWIMV texture analysis relies on a discrete 3D ODF grid (here 5°). Thus, the ODF and pole figure densities in Figs. 5, 6 and 7 with large circular distributions, which should be infinity for single crystals and single spots, are not realistic for a single crystal. Therefore, the approach with a single crystal as described here does not allow the quantitative agreement of orientation or pole densities to be explored. However, the data obtained in this experiment were sufficient to identify the orientation of the crystal and verify the coordinate conventions in *MAUD*, *BEARTEX* and *MTEX*. The changes made in *MAUD* version 2.996 may influence the coordinate systems of data analyzed from other synchrotron and neutron diffraction instruments. It is recommended that researchers verify the consistency of coordinate systems for their particular instrument using a methodology similar to the one described in this paper. To break the symmetry of the detector coverage in other instruments, it is recommended to physically shield or electronically disable detectors at known locations rather than disabling detectors in the software. In addition, it is paramount on changing versions of *MAUD* that the *MAUD* home folder be deleted. It will be regenerated when the *MAUD* program is launched.

7. Conclusions

An approach was presented for verifying coordinate systems used in texture analysis. In the test case, the instrument coordinate system of HIPPO was related to the sample coordinate system using a symmetry-breaking detector layout, thereby identifying issues in the coordinate system conventions programmed in *MAUD*. Corrections were implemented in *MAUD* version 2.996 for this paper and an exhaustive discussion of the *MAUD* coordinate systems is given as a definitive reference. A quartz single crystal was also measured with a clear relationship between the crystal and sample coordinate systems, allowing the sample coordinate system to be validated. Correct coordinate systems are required for the more general case of polycrystalline quantitative texture analysis. In addition, texture software such as *MTEX*, *BEARTEX* and *MAUD* can use different conventions; this work provides practical ways to verify that plotting and crystal conventions are appropriate.

Funding information

This work has benefitted from the use of the Los Alamos Neutron Science Center (LANSCE) at Los Alamos National Laboratory (LANL). LANL is operated by Triad National Security, LLC, for the National Nuclear Security Administration of the US Department of Energy (DOE) (contract No. 89233218NCA000001). HRW acknowledges support from DOE-BES (DE-FG02-05ER15637) and the National Science Foundation (award Nos. EAR 1343908; 2054951; 2154351). We acknowledge support through the LANL Institute for Materials Science (IMS) Rapid Response award for an extended visit by LL to LANL.

References

Bachmann, F., Hielscher, R. & Schaeben, H. (2010). *Solid State Phenom.* **160**, 63–68.
Bunge, H. J. (1969). *Mathematische Methoden der Texturanalyse.* Berlin: Akademie-Verlag.
Bunge, H.-J. & Roberts, W. T. (1969). *J. Appl. Cryst.* **2**, 116–128.
Chateigner, D., Lutterotti, L. & Morales, M. (2019). *International Tables for Crystallography*, Vol. H, edited by C. J. Gilmore, J. A. Kaduk & H. Schenk, p. 572. Chichester: Wiley.
Chen, K., Dejoie, C. & Wenk, H.-R. (2012). *J. Appl. Cryst.* **45**, 982–989.
Coelho, A. A. (2018). *J. Appl. Cryst.* **51**, 210–218.
Gilmore, C. J., Kaduk, J. A. & Schenk, H. (2019). *International Tables for Crystallography*, Vol. H, edited by C. J. Gilmore, J. A. Kaduk & H. Schenk, pp. 698–715. Chichester: Wiley.
Grässlin, J., McCusker, L. B., Baerlocher, C., Gozzo, F., Schmitt, B. & Lutterotti, L. (2013). *J. Appl. Cryst.* **46**, 173–180.
Jennings, S. (2021). *Powder Diffr.* **36**, 212.
Kocks, U. F., Tomé, C. N. & Wenk, H.-R. (1998). Editors. *Texture and Anisotropy, Preferred Orientations in Polycrystals and their Effect on Materials Properties*. Cambridge University Press.
Larson, A. C. & Von Dreele, R. B. (1994). *GSAS*. Report LAUR 86-748. Los Alamos National Laboratory, New Mexico, USA.
Le Page, Y. & Donnay, G. (1976). *Acta Cryst.* B**32**, 2456–2459.
Losko, A. S., Vogel, S. C., Reiche, H. M. & Nakotte, H. (2014). *J. Appl. Cryst.* **47**, 2109–2112.
Lutterotti, L. (2010). *Nucl. Instrum. Methods Phys. Res. B*, **268**, 334–340.
Lutterotti, L., Matthies, S., Wenk, H.-R., Schultz, A. & Richardson, J. Jr (1997). *J. Appl. Phys.* **81**, 594–600.
Matthies, S., Pehl, J., Wenk, H.-R., Lutterotti, L. & Vogel, S. C. (2005). *J. Appl. Cryst.* **38**, 462–475.
Matthies, S., Vinel, G. & Helming, K. (1987). *Standard Distributions in Texture Analysis*. Berlin: Akademie Verlag.

Matthies, S., Wenk, H.-R. & Vinel, G. W. (1988). *J. Appl. Cryst.* **21**, 285–304.
McCusker, L. B., Von Dreele, R. B., Cox, D. E., Louër, D. & Scardi, P. (1999). *J. Appl. Cryst.* **32**, 36–50.
Peterson, N. E., Einhorn, J. R., Fancher, C. M., Bunn, J. R., Payzant, E. A. & Agnew, S. R. (2021). *J. Appl. Cryst.* **54**, 867–877.
Rafailov, G., Caspi, E. N., Hielscher, R., Tiferet, E., Schneck, R. & Vogel, S. C. (2020). *J. Appl. Cryst.* **53**, 540–548.
Rietveld, H. M. (1969). *J. Appl. Cryst.* **2**, 65–71.
Rodríguez-Carvajal, J. (2001). *IUCr Comm. Powder Diffr. Newsl.* **26**, 12–19.
Takajo, S. & Vogel, S. C. (2018). *J. Appl. Cryst.* **51**, 895–900.
Toby, B. H. & Von Dreele, R. B. (2013). *J. Appl. Cryst.* **46**, 544–549.
Ullemeyer, K., Spalthoff, P., Heinitz, J., Isakov, N., Nikitin, A. & Weber, K. (1998). *Nucl. Instrum. Methods Phys. Res. A*, **412**, 80–88.
Vogel, S. C., Hartig, C., Lutterotti, L., Von Dreele, R. B., Wenk, H.-R. & Williams, D. J. (2004). *Powder Diffr.* **19**, 65–68.
Von Dreele, R. B. (1997). *J. Appl. Cryst.* **30**, 517–525.
Wenk, H.-R. & Van Houtte, P. (2004). *Rep. Prog. Phys.* **67**, 1367–1428.
Wenk, H.-R., Lutterotti, L. & Vogel, S. (2003). *Nucl. Instrum. Methods Phys. Res. A*, **515**, 575–588.
Wenk, H.-R., Lutterotti, L. & Vogel, S. (2010). *Powder Diffr.* **25**, 283–296.
Wenk, H.-R., Matthies, S., Donovan, J. & Chateigner, D. (1998). *J. Appl. Cryst.* **31**, 262–269.